RESEARCH ARTICLE

Magnetic Resonance in Medicine

SPARCQ: A new approach for fat fraction mapping using asymmetries in the phase-cycled balanced SSFP signal profile

Giulia M. C. Rossi[1,2,3] | **Adèle L. C. Mackowiak[1,2,3]** | **Berk Can Açikgöz[1,2]** | **Katarzyna Pierzchała[4,5]** | **Tobias Kober[3,6,7]** | **Tom Hilbert[3,6,7]** | **Jessica A. M. Bastiaansen[1,2]**

[1]Department of Diagnostic, Interventional and Pediatric Radiology (DIPR), Inselspital, Bern University Hospital, University of Bern, Bern, Switzerland

[2]Translational Imaging Center, Swiss Institute for Translational and Entrepreneurial Medicine, Bern, Switzerland

[3]Department of Diagnostic and Interventional Radiology, Lausanne University Hospital and University of Lausanne, Lausanne, Switzerland

[4]CIBM Center for Biomedical Imaging, Lausanne, Switzerland

[5]Animal Imaging and Technology, Ecole Polytechnique Fédérale de Lausanne, Lausanne, Switzerland

[6]Advanced Clinical Imaging Technology, Siemens Healthineers International AG, Lausanne, Switzerland

[7]LTS5, École Polytechnique Fédérale de Lausanne (EPFL), Lausanne, Switzerland

Correspondence
Jessica A. M. Bastiaansen, Department of Diagnostic, Interventional and Pediatric Radiology (DIPR), Inselspital, Bern University Hospital, University of Bern, Bern, Switzerland.
Email: jbastiaansen.mri@gmail.com

Funding information
Emma Muschamp; Swiss Heart foundation, Grant/Award Number: FF18054; Swiss National Science Foundation, Grant/Award Number: PCEFP2_194296

Abstract

Purpose: To develop SPARCQ (Signal Profile Asymmetries for Rapid Compartment Quantification), a novel approach to quantify fat fraction (FF) using asymmetries in the phase-cycled balanced SSFP (bSSFP) profile.

Methods: SPARCQ uses phase-cycling to obtain bSSFP frequency profiles, which display asymmetries in the presence of fat and water at certain TRs. For each voxel, the measured signal profile is decomposed into a weighted sum of simulated profiles via multi-compartment dictionary matching. Each dictionary entry represents a single-compartment bSSFP profile with a specific off-resonance frequency and relaxation time ratio. Using the results of dictionary matching, the fractions of the different off-resonance components are extracted for each voxel, generating quantitative maps of water and FF and banding-artifact-free images for the entire image volume. SPARCQ was validated using simulations, experiments in a water-fat phantom and in knees of healthy volunteers. Experimental results were compared with reference proton density FFs obtained with ¹H-MRS (phantoms) and with multiecho gradient-echo MRI (phantoms and volunteers). SPARCQ repeatability was evaluated in six scan-rescan experiments.

Results: Simulations showed that FF quantification is accurate and robust for SNRs greater than 20. Phantom experiments demonstrated good agreement between SPARCQ and gold standard FFs. In volunteers, banding-artifact-free quantitative maps and water-fat-separated images obtained with SPARCQ and ME-GRE demonstrated the expected contrast between fatty and non-fatty tissues. The coefficient of repeatability of SPARCQ FF was 0.0512.

Conclusion: SPARCQ demonstrates potential for fat quantification using asymmetries in bSSFP profiles and may be a promising alternative to conventional FF quantification techniques.

KEYWORDS

3 T, balanced steady-state free precession, bSSFP, PDFF, phase-cycling, profile asymmetry, proton density fat fraction, quantitative MRI, water-fat quantification

1 | INTRODUCTION

Accurate fat quantification is crucial for a variety of clinical applications, including the evaluation of liver steatosis,[1–3] fatty infiltration in the myocardium which is associated with heart failure,[4,5] the relationship between osteoporosis and bone marrow adiposity,[6,7] and characterization of cellularity for radiation dosimetry in cancer patients.[8] Non-invasive fat quantification by MRI has improved patient comfort by avoiding invasive biopsies, which are prone to sampling errors and are highly invasive, limiting their usage in obtaining prognostic information.[4]

Fat quantification can be achieved by quantitative proton density fat fraction (PDFF) methods such as single-voxel MRS, or chemical-shift-based water-fat imaging such as multiecho Dixon MRI.[9–14] Multiecho techniques rely on the acquisition of multiple echoes and require advanced signal processing for robust water-fat separation and quantification.[12,15–17] Multiparametric mapping techniques have been combined with multiecho sampling to enable fat quantification, with promising results.[18–21] Although powerful, PDFF quantification using multiecho methods can be confounded by T_1 bias,[22,23] the assumption of a single T_2^* decaying component,[24] the use of a predetermined spectral fat model,[2,22,25] and the inherent low SNR of gradient-echo based sequences.

Balanced SSFP (bSSFP) sequences provide high SNR and image contrast in relatively short scan times.[26] However, the bSSFP signal is extremely sensitive to off-resonance effects,[27] either due to magnetic field inhomogeneities or chemical shift. This sensitivity is severe for frequencies around 1/TR and may cause signal nulling in the images known as banding artifacts,[28] which can be mitigated by acquiring multiple bSSFP images,[29–33] each with a different phase increment. Measurement of the bSSFP frequency response via phase-cycling, that is phase-cycled bSSFP, revealed profile asymmetries that indicated the presence of multiple tissue components (e.g., different types of tissue) within voxels.[34] Such asymmetries were observed in gray matter, white matter, and muscle,[34–36] were stronger at high magnetic fields,[37] and can be avoided by reducing TR.[38] Profile asymmetries were used to obtain diffusion metrics,[39] and recent work suggests an interplay between the contributions of microstructural, chemical shift, and chemical exchange effects to the asymmetry of the bSSFP profile.[40] Although phase-cycled bSSFP was used for water-fat signal separation,[41–45] its potential to quantify fat by analyzing profile asymmetries has not been investigated.

The aim of this work was to develop a novel quantitative method for measuring fat fraction (FF) using bSSFP Signal Profile Asymmetries for Robust multi-Compartment Quantification (SPARCQ). By using asymmetries in bSSFP profiles, this method has the potential to overcome the limitations of current techniques. The proposed approach was tested in simulations, FF phantoms, and healthy volunteers, and was compared with reference standard PDFF approaches such as ^{1}H-MRS and multiecho GRE techniques.

2 | METHODS

2.1 | SPARCQ acquisition

To measure phase-cycled bSSFP signal profile asymmetries, the SPARCQ acquisition (Figure 1A) consists of multiple ($N = 36$) bSSFP acquisitions, each with a different linear RF phase increment φ_j according to:

$$\varphi_j = \frac{2\pi}{N}(j-1), \qquad j = 1, 2, \ldots, N \qquad (1)$$

Fully-sampled 3D Cartesian data were acquired using slab-selective excitation with the following parameters: TR/TE = 3.4/1.7 ms, RF excitation angle $\alpha = 35°$, a matrix size of 84×112, a FOV of 168×224 mm,^{2} with sufficient slices to cover the volume of interest, an isotropic resolution of $(2\,\text{mm})^3$, and a receiver bandwidth of 930 Hz/px. A TR of 3.4 ms was deliberately chosen to maximize the difference between bSSFP profiles of water and fat at 3T (Figure S1 in Data S1), see also Mackowiak et al.[46] More intuitively, with a TR of 3.4 ms, the locations of the water and main fat peak will wrap into the obtained off-resonance frequency spectrum (Figure 1D) in such a way, that their relative distance is maximized. The choice of TR is fundamental in preventing signals from different components to overlap when wrapping in the [0, 1/TR] range.

At the beginning of each phase-cycled acquisition, 10 ramp-up pulses were applied with linearly increasing RF power.[47] The total acquisition time was 20:35 min. Magnitude and phase images were reconstructed on the scanner and DICOM files were exported.

2.2 | SPARCQ reconstruction

The SPARCQ reconstruction can be divided into five steps that were all implemented in Matlab 8.5 (MathWorks, Natick MA):

1 Construction of a complex bSSFP profile for each voxel using measured data (Figure 1A,B).
2 Creation of a dictionary containing simulated phase-cycled bSSFP profiles. Each entry in the dictionary has
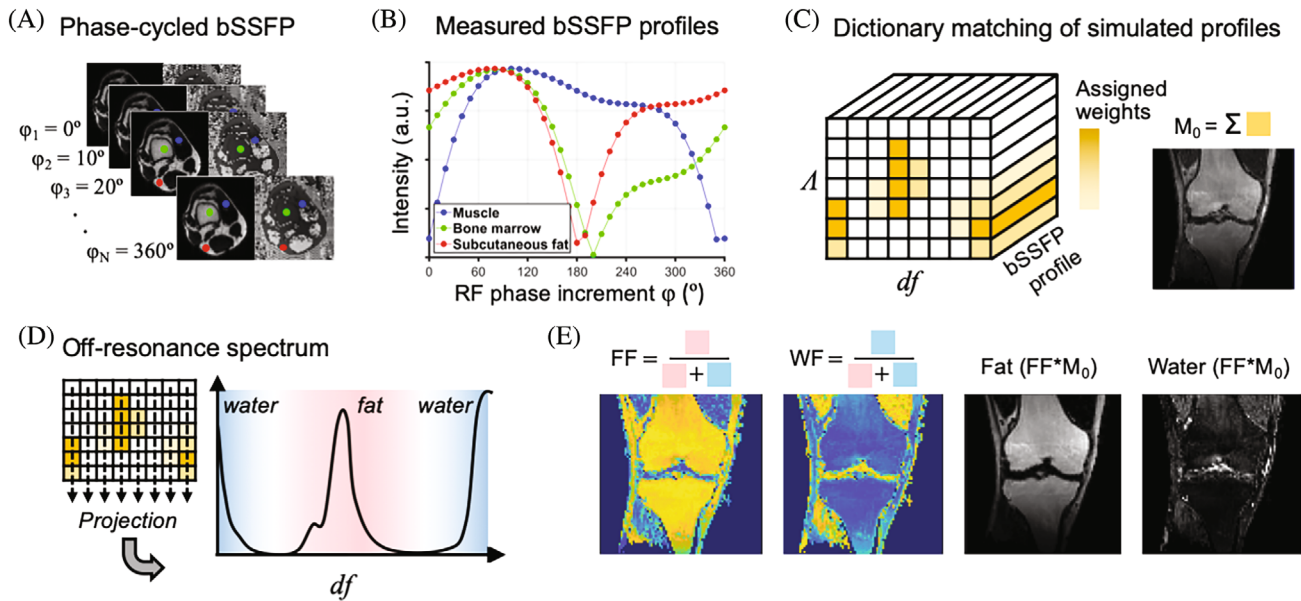
FIGURE 1 Overview of the SPARCQ framework. (A) A phase-cycled bSSFP acquisition is performed and for each voxel. (B) A complex bSSFP profile is obtained (B). (C) A dictionary of simulated bSSFP signal profiles is constructed, to which the measured bSSFP profile is matched, resulting in a weight matrix. Each weight represents the contribution of the corresponding simulated dictionary entry to the acquired profile. (D) The equilibrium magnetization (M_0) is estimated by summing all the weights in the weight matrix. df spectra are obtained by projecting the weight matrix. The FF is computed as the integral over the frequency range assigned to this component (panel D, red background) divided by the sum of the integrals of fat and water. Applying the same procedure to the whole imaging volume allows one to obtain quantitative maps. M_0-weighted images for fat and water are obtained by multiplying the fraction maps by the M_0 map.

a specific off-resonance frequency df and a relaxation time ratio Λ (T_1/T_2) (Figure 1C).

3. Matching of measured bSSFP profiles to a dictionary via a sum of simulated bSSFP profiles (Figure 1C).
4. Computation of df distributions based on obtained weights (Figure 1D).
5. Extraction of water and FF maps and images (Figure 1E).

2.2.1 | Step 1 – Measurement and extraction of complex phase-cycled bSSFP profiles

Complex images were formed from the magnitude and phase DICOM images for each of the N scans. For each voxel, the complex bSSFP profile was then obtained by taking the complex values as function of applied phase increment (Figure 1A,B).

2.2.2 | Step 2 – Creation of the dictionary

The dictionary contains a simulated phase-cycled bSSFP profile for each combination of relaxation time ratio Λ and off-resonance frequency df, resulting in a 2D dictionary (Λ, df) of bSSFP profiles. Profiles were simulated using the Bloch equations with RF phase

increments φ_j, TR, TE, and RF excitation angle α that are identical to the sequence parameters (Section 2.1). The resolution of the dictionary was manually tuned. When approaching the limit $TR/T_2 \to 0$, relaxation time properties enter the dictionary uniquely via their ratio Λ, which was varied from 1 to 26 in steps of 5. This results in a wide enough range of T_1 and T_2 values, so that the water and fat relaxation times are both represented. The off-resonance dimension df included any frequency within the detectable $1/TR$ range, from 0 Hz to $1/TR \sim 294$ Hz in 8 Hz steps. This dimension represents both contributions from magnetic field inhomogeneities and chemical shift. Constraints on chemical shifts and peak amplitudes, such as those used in multi-echo approaches, were not used. Instead, the distinction between water and fat is made based on their matched position in the off-resonance dimension.

2.2.3 | Step 3 – Dictionary matching

The presence of different tissue fractions shapes the measured bSSFP profile, which is a complex sum of individual bSSFP profiles, providing a means of extracting fractional information. However, hardware-related factors can introduce an offset between the phase of the acquired bSSFP profile and the phase of the best dictionary fit, creating

discrepancies between measured and simulated profiles, which may affect dictionary matching accuracy. To address this issue, a phase augmentation step is performed to guide the final matching process. Following the fingerprinting approach,[48] the profile that minimizes the dot product between the dictionary entry and the acquired bSSFP profile is selected, and the median difference with the phase profile of the acquired bSSFP profile is used to augment the phase of the acquired profile. Phase augmentation is a rapid initial estimation, which does not require high precision. Moreover, it has negligible influence on FF estimation (Methods S1 and Figure S4 in Data S1).

Next, the complex bSSFP profile is expressed as a weighted sum of dictionary entries. This approach allows detecting multicompartment compositions within each voxel and provides information on the contribution of each dictionary entry to the measured signal. This technique builds upon previous work on myelin-water imaging,[49,50] but extends it to two dimensions, Λ and df. To accomplish this, a 2D weight matrix, the same size as the dictionary, is defined in which each cell represents the weighting of the corresponding dictionary entry (Figure 1C).

All profiles are expressed as a concatenation of their real and imaginary parts, to guarantee real-valued weights, doubling the length of each signal to $2N$. To further simplify the fitting, the 2D dictionary of bSSFP profiles and the 2D weight matrix are reshaped to a $2N \times k$ matrix for the dictionary and a $k \times 1$ vector for the weights. Where k has length of 216 (6 Λ values $\times$ 36 df values). By naming s_{acq} the $2N \times 1$ acquired signal, $\mathbf{D}$ the $2N \times k$ reshaped dictionary and $\mathbf{w}$ the $k \times 1$ reshaped weight matrix, the optimization problem can be mathematically described as follows:

$$\hat{\mathbf{w}} = \underset{\mathbf{w}}{\operatorname{argmin}} \left\{ \|\mathbf{D} \cdot \mathbf{w} - s_{acq}\|_2^2 + \lambda \|\mathbf{\Delta w}\|_2^2 \right\}$$
$$\text{subject to } \mathbf{w} \geq 0 \quad (2)$$

The L_2 norm was chosen as a distance metric and the constraint $\mathbf{w} \geq 0$ was added to avoid negative weights that would hinder finding a biologically plausible solution. Therefore, the first term corresponds to a classical non-negative least-squares (NNLS) problem. Since the problem is ill-posed and prone to overfitting, a second order Laplacian regularization term was added to favor smoothness between neighboring weights $\mathbf{\Delta w}$, as described previously.[49,50] The solution of the NNLS problem is the $k \times 1$ array of weights, which can be used to compute the $2N \times 1$ best fit signal given by the weighted sum of all the signals in the dictionary ($\mathbf{D} \cdot \mathbf{w}$). The final weight matrix is obtained by representing the array of weights in its original 2D shape, with relaxation time ratio and off-resonance frequencies as dimensions.

The regularization parameter was manually tuned and tested (Figure S5 in Data S1) and set to 0.08 in phantom experiments and to 0.025 in volunteer experiments.

Consequently, the sum of the weights in a voxel does not necessarily add up to 1, but to the total signal intensity in that voxel. The weights only represent the relative contribution of each compartment to the total signal. It is important to note that the signals are not normalized in the multicompartment fitting step, as this can introduce errors in the estimation of the weights.

2.2.4 | Step 4 – Estimation of off-resonance spectra

The weight matrix contains information on the voxel content in terms of relaxation time ratios and off-resonance frequencies. To visualize the off-resonance information, distributions of the off-resonance frequency content are obtained by projecting the weight matrix onto the axis of off-resonance frequencies (Figure 1D).

2.2.5 | Step 5 – Quantitative parameter mapping and qualitative image reconstruction

The composition of a given voxel can be extracted from the obtained spectrum (i.e., distribution of weights). For a two-compartment system, the fraction of one tissue component with a specific frequency range (e.g., fat) can be computed as the integral of the projected df spectrum over the frequency range assigned to it, divided by the sum of the integrals over the frequency ranges assigned to the first and second component (Figure 1E).

In the case of water-fat separation, the FF and water fraction (WF) are defined as:

$$FF = \frac{F}{F + W} \quad (3)$$

$$WF = 1 - FF \quad (4)$$

Where F and W are the integrals of the df spectrum over the frequency ranges assigned to fat and water, respectively.

To account for small frequency shifts caused by local magnetic field inhomogeneity, the peak that is closest to either 0 Hz or 1/TR is assigned to water. The spectrum is then shifted along the off-resonance axis so that the assigned water peak is centered around 0 Hz. Next, the position of the fat peak is determined, which is defined as the peak with the largest amplitude between 0 and 1/TR. The first minima between the water and the fat peak are used as integration limits to obtain F and W.

In a voxel, the thermal equilibrium magnetization M_0 can be estimated as a weighted sum of each dictionary entry since the weight matrix gives an estimation of the contribution of each signal in the dictionary to the acquired signal. As the signals in the dictionary were all simulated for $M_0 = 1$, the thermal equilibrium magnetization in a voxel can be estimated as the sum of all weights in the matrix.

Application of the framework over the whole volume (N.B.: step 2 of dictionary creation only needs to be completed once for the whole volume), quantitative maps of FF, WF, and equilibrium magnetization M_0 can be obtained (Figure 1F).

The framework allows the extraction of qualitative images of individual components that may be easier to interpret (Figure 1F). To do this, M_0-weighted images for each component can be obtained by voxel-wise multiplication of the corresponding fraction maps, in the current case WF or FF, with the M_0 map.

2.3 | Numerical simulations

Numerical simulations were performed to evaluate the accuracy of SPARCQ for FF quantification and to test its robustness in the presence of noise.

First, ^{1}H NMR spectra were simulated that consisted of a single water peak resonating at 0 Hz and two fat peaks at -485 and -434 Hz, with a relative 1:4 peak area ratio. Each peak was modeled as a Lorentzian function with a FWHM of 20 Hz according to

$$L(x) = \frac{A}{1 + x^2} \quad \text{with} \quad x = \frac{2(P - P_0)}{\text{FWHM}} \qquad (5)$$

with A the peak area, P the frequency ranging from -600 to 200 Hz with steps of 1 Hz, and P_0 the center frequency. The three peak areas were adjusted for different FF ranging from 0 to 1 in steps of 0.05. Then, the three Lorentzian line shapes were summed to obtain a set of simulated ^{1}H spectra for each FF.

Second, Bloch simulations were performed to generate bSSFP signal profiles for each frequency of the simulated ^{1}H spectra. Off-resonance frequencies were varied from -600 to 200 Hz (in steps of 1 Hz), with all other parameters being fixed (TR = 3.40 ms, TE = 1.7 ms, $\alpha = 35°$, $\Gamma = 6$ [$T_1 = 480$ ms, $T_2 = 80$ ms]). To obtain a final complex bSSFP profile for each FF, the simulated bSSFP profiles were weighted by the amplitude of their corresponding off-resonance frequency in the simulated ^{1}H spectrum and summed.

Third, randomly generated white Gaussian noise (SNR levels ranging from 5 to 100 in steps of 2.5) was added to the imaginary and real part of each bSSFP profile. SPARCQ

was used for FF estimation in each of the generated bSSFP profiles. The experiment was iterated 100 times, using a different seed at each iteration for the randomly generated noise. The mean and SD of the estimation error over the 100 iterations were calculated.

The numerical simulations were repeated for Dirac-shaped ^{1}H NMR spectra (Figure S2 in Data S1), for the use of different relaxation time ratios of water and fat ($\Lambda = 1$ for fat and $\Lambda = 21$ for water, Figure S3), and to confirm the negligible effect of the phase augmentation step on FF estimates (Methods S1 in Data S1).

2.4 | FF phantom experiments at 3T and 9.4T

The accuracy of the proposed framework was evaluated in phantoms. First, a dedicated fat-water phantom was created[51] composed of six 50 mL Falcon tubes with different partial volumes of peanut oil (0%, 20%, 40%, 60%, 80%, 100%) immersed in a 3% weight agar solution (Figure 4C). Peanut oil was chosen because it has resonance frequencies similar to those of triglycerides in human adipose tissue.[25] To quantify the PDFF, unlocalized ^{1}H MRS was performed separately in each Falcon tube in a 9.4T MRI scanner (Magnex Scientific, Oxford, UK) with a Direct Drive spectrometer (Agilent, Palo Alto, CA, USA). Line shape fitting and integration in jMRUI4.0 was used to calculate the peak areas of all visible resonances and obtain the gold standard FF(GS). In addition, a chemical shift thresholded (CST) FF was quantified for each tube. The CST method assigns resonance peaks between 3.5 and 6.0 ppm to water and resonance peaks between 0 and 3 ppm to fat. It was used as an additional metric for comparison because the current SPARCQ implementation assigns resonance peaks of fat close to the water resonance to the water compartment. This additional metric evaluates SPARCQ for tissue fraction quantification prior to using potential correction methods such as a six-peak fat model.[25]

Phantom acquisitions were performed on a clinical 3T scanner (MAGNETOM Prisma$^{\text{fit}}$, Siemens Healthcare, Erlangen, Germany) using a commercially available 18-channel body coil. A prototype 3D Cartesian phase-cycled bSSFP sequence (Section 2.1) and a reference multiecho GRE (ME-GRE) sequence were used for data acquisition. ME-GRE acquisition parameters were: 13 monopolar echoes with TEs from 1.34 to 25.10 ms and an echo spacing of 1.98 ms, an isotropic resolution of $2.0 \times 2.0 \times 2.0$ (mm)^3, RF excitation angle of 20°, a receiver bandwidth of 970 Hz/pixel, and an acquisition time of 3:02 min. ME-GRE data were processed with the ISMRM Fat-Water Toolbox[15,16] to obtain FFs, using a nine-peak fat spectral model determined by the 9.4T MRS experiments.

B_0 field maps provided by the Toolbox were used to estimate magnetic field inhomogeneity.

FFs were quantified in manually drawn regions of interest (ROIs) corresponding to the six vials. FF obtained with SPARCQ and ME-GRE were compared with the gold standard FF determined with ^{1}H MRS at 9.4T. ROIs were chosen to span five consecutive slices for comparability with unlocalized spectroscopy data. To focus on accuracy of SPARCQ and not on its sensitivity to B_0 inhomogeneities, the five slices per vial were chosen in regions where B_0 inhomogeneities in the agar surrounding the vials was as small as possible. Additional analyses were performed to determine the impact of B_0 inhomogeneities on SPARCQ-based FF estimates, and to identify sources of error that can be mitigated in future implementations. To test this, B_0 information extracted from the ME-GRE scans was used to shift the acquired phase-cycled bSSFP profiles prior to dictionary matching (Methods S2 in Data S1).

2.5 | Volunteer experiments

Volunteer experiments were performed in knees using a commercially available 15-channel Tx/Rx knee coil (Quality Electrodynamics, Mayfield, OH, USA) at the same clinical 3T scanner as described before. The volunteers gave written and informed consent. The study was carried out according to institutional rules.

2.5.1 | Scan-rescan repeatability study in volunteers

A scan-rescan repeatability study was performed on six human knees, with repositioning in between scans. For reference, a Dixon acquisition was performed with a turbo spin echo (TSE) Dixon sequence with TR/TE = 3470/100 ms, RF excitation angle $\alpha = 150°$, matrix size 128×80, FOV 160×256 mm, isotropic resolution $(2\,\text{mm})^3$, receiver bandwidth 601 Hz/px, and turbo factor 18. In-phase, out-of-phase, water, and fat images were reconstructed on the scanner.

Quantitative maps were obtained with SPARCQ as described. A thresholding was performed based the amplitude range of the profile, which was performed to mask the background and voxels with low signal.

Spectra and estimated parameters were checked in areas close to air-tissue interfaces (e.g., patella) to evaluate the efficacy of SPARCQ in regions of strong B_0 inhomogeneity. Bland–Altman analysis was performed on the scan-rescan data on the mean FFs obtained with SPARCQ in elliptical ROI in five different tissues (vastus

medialis, biceps femoralis, semimembranous muscles, bone marrow, and subcutaneous fat). Water-fat-separated images obtained with SPARCQ were compared with those obtained with Dixon scans.

2.5.2 | Comparison with ME-GRE

A comparison was made between the FF estimates obtained with SPARCQ and ME-GRE on two human knees. Phase-cycled bSSFP scans as well as ME-GRE scans were performed as described earlier. For data processing with the ISMRM Fat-Water Toolbox, a six-peak fat spectral model was used.[25] Quantitative maps were obtained with SPARCQ and ME-GRE, and a Bland–Altman analysis was performed on the mean FF obtained with SPARCQ and ME-GRE in elliptical ROIs in five different tissues (vastus medialis, biceps femoralis, semimembranous muscles, bone marrow, and subcutaneous fat).

3 | RESULTS

3.1 | Numerical simulations

The bSSFP signal profiles (Figure 2B, only magnitude is shown) obtained from simulated ^{1}H MR spectra (Figure 2A) show a clear difference in shape when the FF is changed from 0 to 1, whereas signals from mixed water and fat display large asymmetries. The off-resonance frequency spectra (Figure 2D) derived from the weight matrix (Figure 2C) correlate well with the simulated spectra. It should be noted that, although the simulated spectra cover a large frequency range, the spectra derived from SPARCQ are limited to the range 0–1/TR. Therefore, a wrapping of the spectra can be observed. The fat resonance frequencies around −440 Hz in the simulated spectra are found at around 150 Hz in the off-resonance frequency spectra derived from the fitting. This is reasonable, since unwrapping the phase advance accumulated in a TR of 3.4 ms for a frequency of −440 Hz leads to a phase advance of 178°, corresponding to a frequency of 148 Hz.

The FFs estimated with SPARCQ (Figure 3A) in the presence of different noise allowed to evaluate the accuracy and noise robustness of the proposed algorithm. The mean fitting error and its SD over the 100 repetitions (Figure 3B and Figure 3C) showed that strong noise (SNR < 20) leads to reduced accuracy (Figure 3B) and precision (Figure 3C), which is confirmed by both the higher mean and the higher SD of the error over repetitions. In noisy signals (SNR < 10), small FFs (∼0.2) seem to be more accurately estimated than higher ones (∼0.8), the latter demonstrating severe underestimations. For
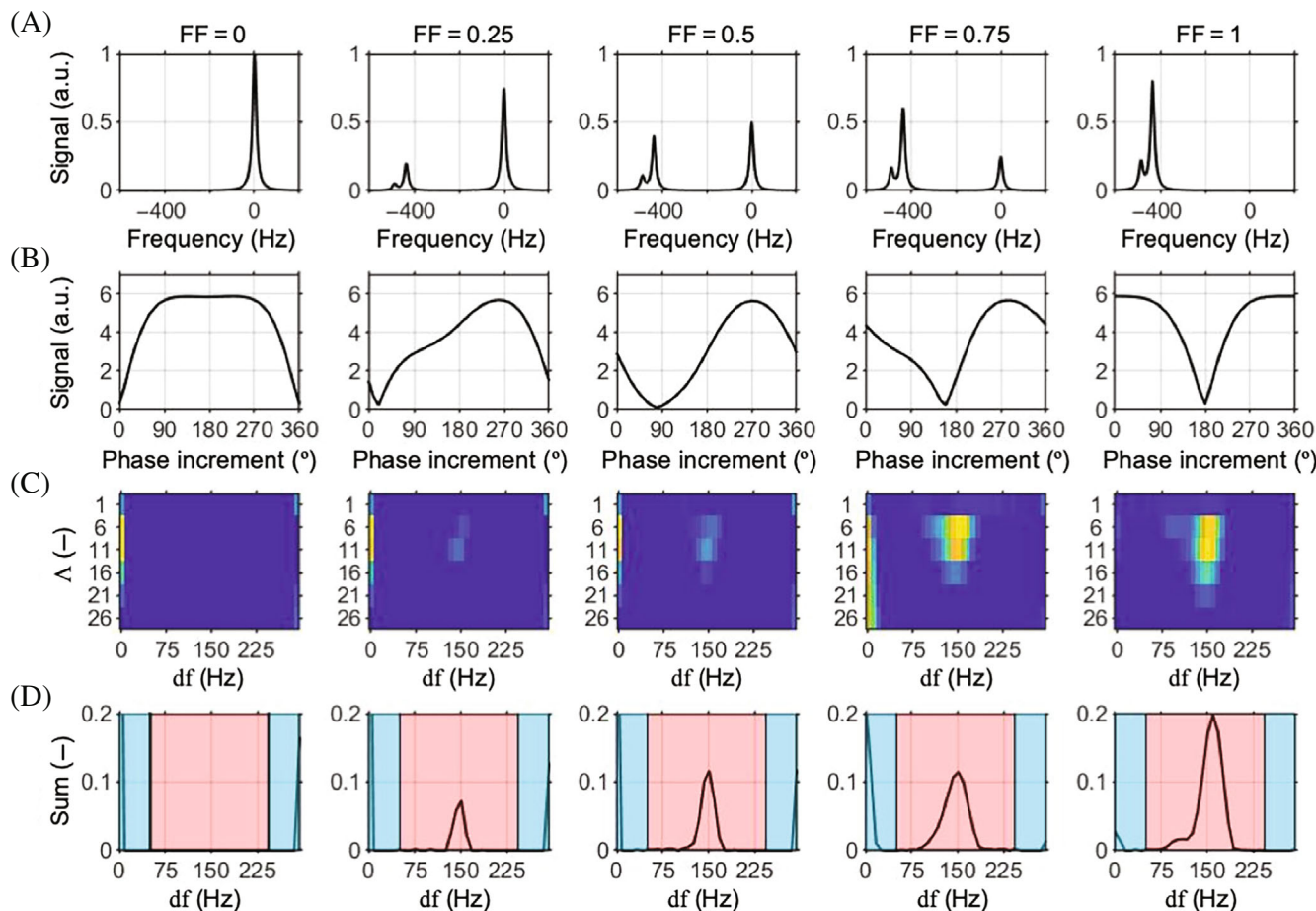
FIGURE 2 Simulation experiment. (A) ^{1}H MR spectra were simulated in the frequency range −200 to 600 Hz for FFs going from 0 to 1 in steps of 0.25. (B) The corresponding phase-cycled bSSFP signal profiles were simulated (magnitude). Following dictionary matching, (C) weight matrices are obtained, (D) which are used to obtain off-resonance frequency spectra with a bandwidth ranging from 0 to 1/TR. The locations of water and fat peaks (C, D, respectively) are wrapped within a 1/TR frequency range.
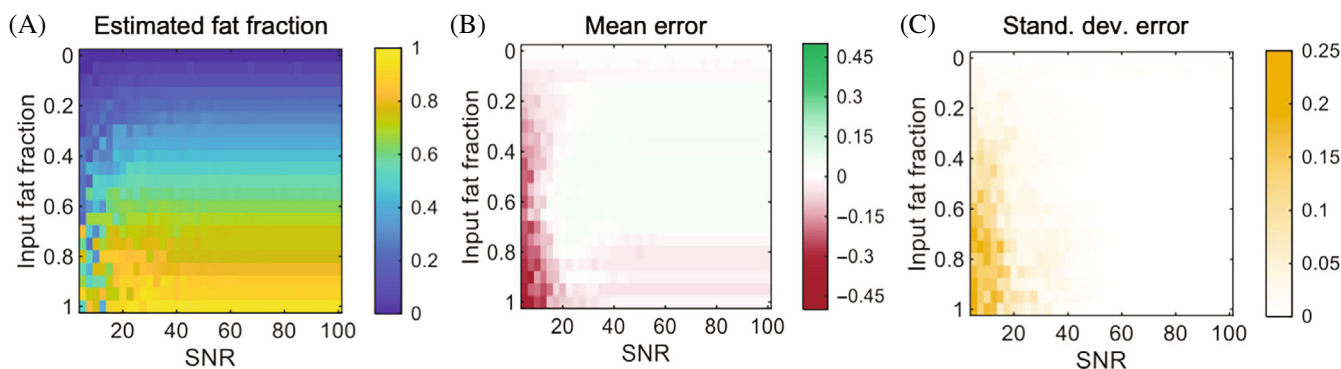
FIGURE 3 Simulation experiments to test the noise robustness of SPARCQ. (A) FFs estimated with SPARCQ depending on the SNR. (B) Mean error of the FF estimation (estimated-input) depending on the SNR for 100 repetitions. (C) SD of the FF estimation error depending on the SNR for 100 repetitions.

higher SNR (>20) estimations gain in both accuracy and precision. However, small underestimations (for FF >0.7 and FF <0.15) or overestimations (for 0.15 < FF <0.7) were observed.

Using Dirac-shaped spectra instead of Lorentzian shapes with a FWHM of 20 Hz had slight effects on simulated bSSFP profiles and FF estimates (Figure S2 in Data S1). Changing the relaxation time ratios T1/T2 of
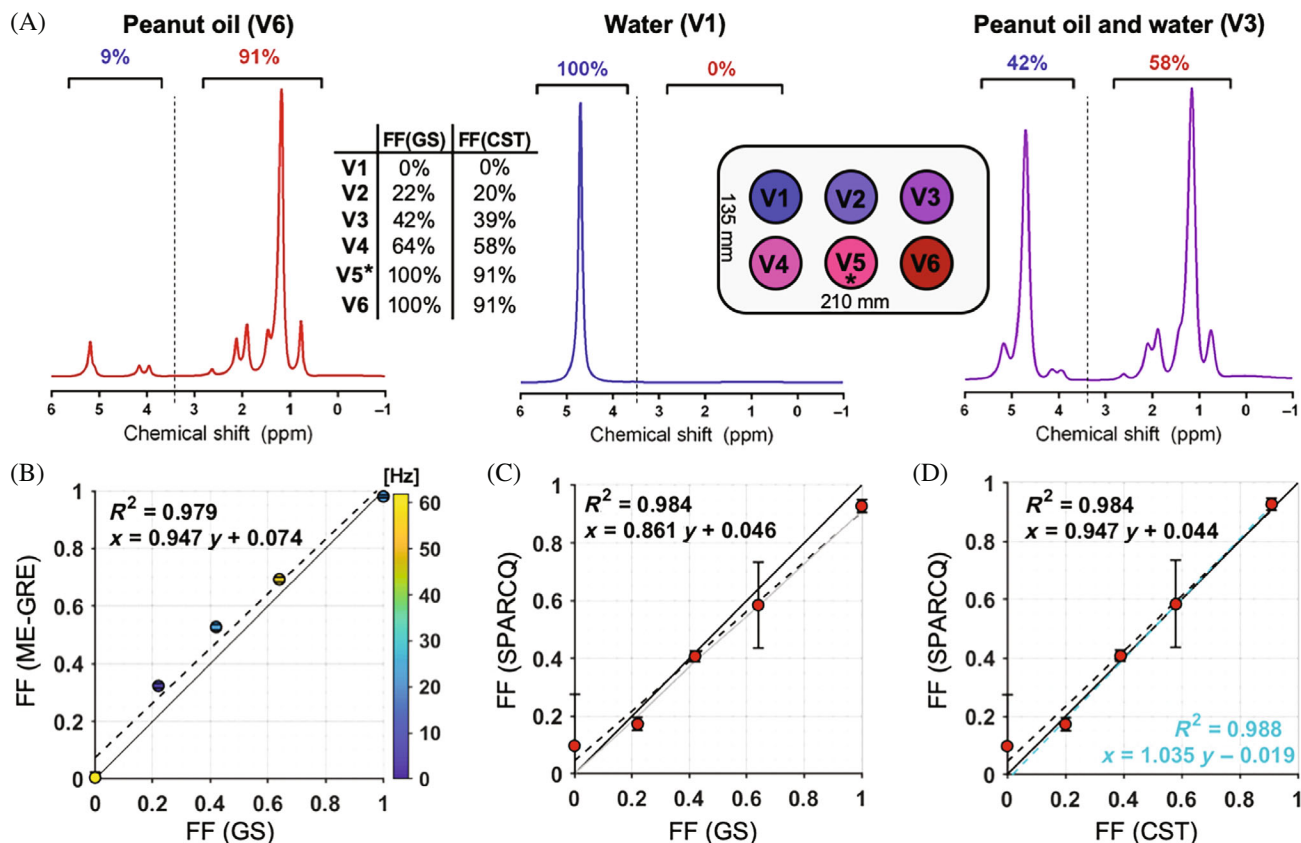
FIGURE 4 Accuracy of SPARCQ. (A) Example of ^{1}H MR spectra obtained at 9.4T for three vials in the fat phantom. Peak areas were obtained for all visible resonances using jMRUI, which were then used to calculate the gold standard PDFF, FF(GS), and a chemical shift threshold FF, FF(CST). For FF(CST), resonances above 3.5 ppm were assigned to water, below 3.5 ppm to fat (dashed vertical line in panel A). FFs estimated with (B) ME-GRE and (C, D) SPARCQ in each vial versus FF(GS) and FF(CST). The unit line (solid black line) and the regression line (dashed black line) are also plotted. (B) The color code indicates the mean B_0 field inhomogeneity (in Hz) within the ROI considered. Field inhomogeneity is the cause for the SPARCQ FF deviation (vial V1) and increase in SD (vial V4). (D) The light blue regression line was obtained by weighting each sample by the inverse of the mean B_0 field inhomogeneity. *V5 was excluded because of water–oil phase separation shortly after phantom building.

both water and fat appeared to have minor effects on FF estimates using SPARCQ (Figure S3 in Data S1).

3.2 | Phantom experiments at 3T and 9.4T

^{1}H spectra acquired at 9.4T in the different Falcon tubes showed well-resolved resonance frequencies (Figure 4A). Besides one tube, which was excluded, all phantom components formed neat agar emulsions without phase separation of water and oil. The gold standard FFs, FF(GS), determined with ^{1}H MRS, were 0%, 22%, 42%, 64%, and 100%. The corresponding fractions assigned using a chemical shift threshold, FF(CST), were 0%, 20%, 39%, 58%, and 91%, respectively.

FF quantification with ME-GRE agreed well, with a regression line FF(ME-GRE) = 0.947 × FF(GS) + 0.074 (Figure 4B). SPARCQ FF quantification (Figure 4C)

showed good agreement with a regression line FF(SPARCQ) = 0.861 × FF(GS) + 0.046 (Figure 4E), and a regression line FF(SPARCQ) = 0.947 × FF(CST) + 0.044 (Figure 4D). The observed deviation is mainly driven by vial V1, which had a strong B_0 field inhomogeneity (~60 Hz) (Figure 4B, color bar). A B_0-weighted regression (Figure 4D, blue regression line) allowed to correlate the lower precision and higher SD of FFs estimated with SPARCQ in vial V1 and V4 to B_0 field inhomogeneities.

3.3 | Volunteer experiments

All quantitative maps (Figures 5A and 6) and water-fat-separated images (Figure 5B) obtained with SPARCQ demonstrated the expected contrast between fatty (bone marrow, subcutaneous fat) and non-fatty (muscles) tissues. In peripheral regions close to air-tissue interface (e.g., patella), an inverted contrast may be
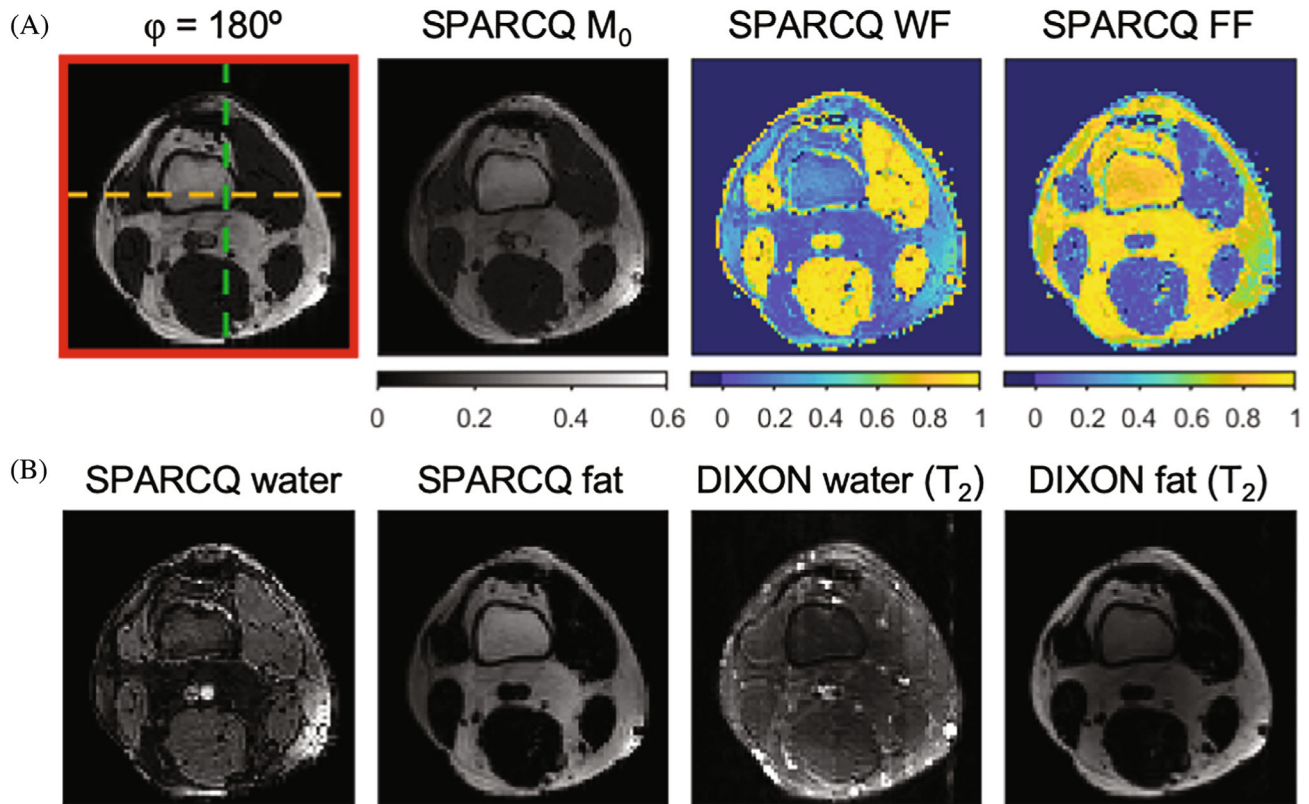
FIGURE 5 Quantitative maps and water-fat-separated images. Example images of one volunteer. (A) Quantitative maps obtained with SPARCQ in an axial view. (B) M_0-weighted water-fat-separated images obtained with SPARCQ and T2-weighted water-fat-separated images obtained with TSE Dixon (TR/TE = 3470/100 ms, resolution (2 mm)^3, receiver bandwidth 601 Hz/px, turbo factor 18; in-phase, out-of-phase, water and fat images were reconstructed on the scanner). Figure S6 in Data S1 shows the axial, sagittal, and coronal views of this data set.
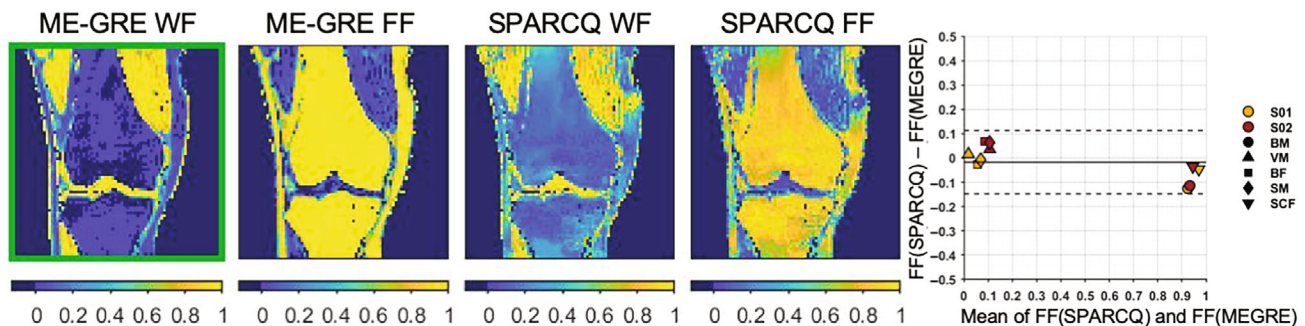
FIGURE 6 Quantitative water and FF maps obtained with phase-cycled bSSFP (SPARCQ) and multiecho GRE (ME-GRE) in one volunteer. Bland-Altmann analysis of FFs estimated with SPARCQ and ME-GRE in two volunteers (one volunteer = one color) for five regions of interest (one marker type = one region). Limits of agreement: LOA = −0.0170 ± 1.96 × 0.0665. BM, bone marrow; BF, biceps femoralis; SCF, subcutaneous fat; SM, semimembranous muscle; VM, vastus medialis. Figure S7 in Data S1 shows the axial, sagittal and coronal views of this data set. The current SPARCQ implementation does not consider B_0 inhomogeneities, resulting in variations close to air interfaces.

observed (Figure S6 and S7 in Data S1). Despite the difference in contrast in water-fat-separated images obtained with SPARCQ (M_0 weighting) and with Dixon (T2 weighting) (Figure 5B), SPARCQ fat and Dixon fat images were in good agreement based on a visual assessment. In water images, hyperintensities were observed in the same structures filled with liquid.

Quantitative maps obtained with SPARCQ and ME-GRE (Figure 6) were in agreement, with ME-GRE showing more polarized (i.e., 100% fat or 100% water) estimations. In peripheral regions close to the air-tissue interfaces (e.g., patella, Figure S7 in Data S1), ME-GRE outperformed SPARCQ. Bland-Altmann analysis on the FF maps estimated with SPARCQ and ME-GRE (Figure 6) revealed
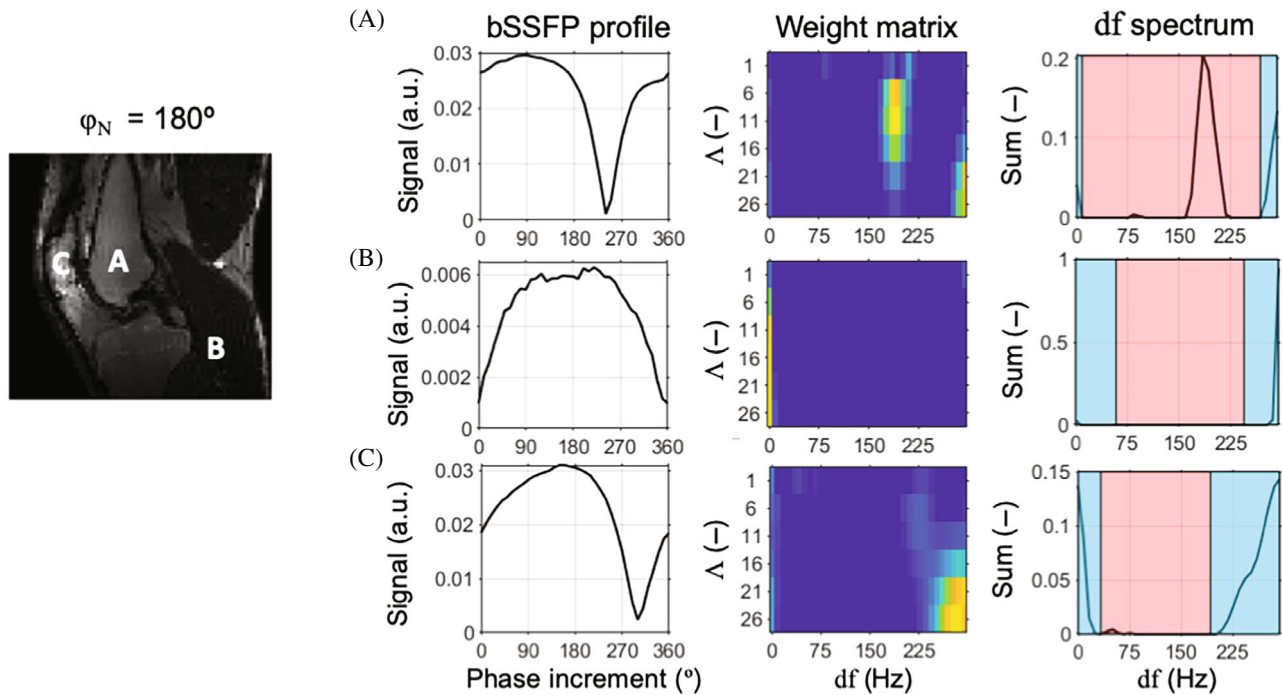
FIGURE 7 Dictionary matching results in three voxels belonging to different tissues. Acquired bSSFP signal profiles (left column), optimized weight matrices (middle column), and off-resonance frequency spectra (right column) for a voxel belonging to fatty (bone marrow, A), non-fatty (muscle, B) tissue, and a voxel close to the air-tissue interface (patella, C). The df spectrum (right) is obtained by projecting the weight matrix onto the df axis (SOW, sum of weights). The selected ranges of tissue-specific frequencies are marked blue (fat) and red (water). (A) In bone marrow, multiple frequency components are detected (on-resonant water, off-resonant fat). (B) In muscle, a single frequency component (on-resonant water) is detected. (C) Close to the air-tissue interface, the peak in the df spectrum is wrongly assigned to water presumably due to large B_0 field inhomogeneity. Figure S8 in Data S1 demonstrates the capability of SPARCQ when such B_0 effects can be mitigated.

limits of agreement (LOA) of $-0.0170 \pm 1.96 \times 0.0665$ between the two methods, with greater disagreement in voxels where SPARCQ was estimating more mixed tissue compositions (e.g., bone marrow).

Off-resonance frequency spectra obtained from the weight matrices in fatty regions (Figure 7A) and non-fatty regions (Figure 7B) far from the air-tissue interface showed the expected frequency components: a narrow on-resonant peak corresponding to water, and a broader off-resonant peak corresponding to fat. On the other hand, in a region near an air-tissue interface (as shown in Figure 7C), water and fat were misclassified due to local B_0 inhomogeneity and the rigid assignment of the water peak in the current implementation.

FFs in ROIs in different tissues (Figure 7B) showed good agreement between all the subjects, with muscles showing a low fat content ($3.2 \pm 0.9\%$ vastus medialis, $7.3 \pm 2.8\%$ biceps femoralis, $5.8 \pm 1.5\%$ semimembranous muscles) and bone marrow and subcutaneous fat confirming their high fat content ($81.7 \pm 2.4\%$ bone marrow, $94.3 \pm 0.9\%$ subcutaneous fat).

The Bland-Altmann analysis on the FF maps in the scan-rescan experiment (Figure 8) revealed very low

bias, $b = 0.0074$, and a good coefficient of repeatability, $CR = 0.0512$.

4 | DISCUSSION

This work presents a novel quantitative method for detecting different tissue compartments based on phase-cycled bSSFP profile asymmetries. SPARCQ estimates off-resonance frequency spectra from acquired bSSFP profiles in each voxel. The obtained spectra reveal the presence of different tissue compartments, such as water and fat, and allow the quantification of their individual contribution to the overall signal profile within the same voxel. In addition, SPARCQ provides an estimation of the equilibrium magnetization M_0, enabling the generation of distinct M_0-weighted images for each component, free of banding artifacts.

The proposed SPARCQ framework was evaluated for FF mapping by comparing it to reference standards for PDFF, such as high resolution ^1H MRS and multiecho GRE. In phantom studies, both the ME-GRE and SPARCQ methods provided FF estimates that were equally close
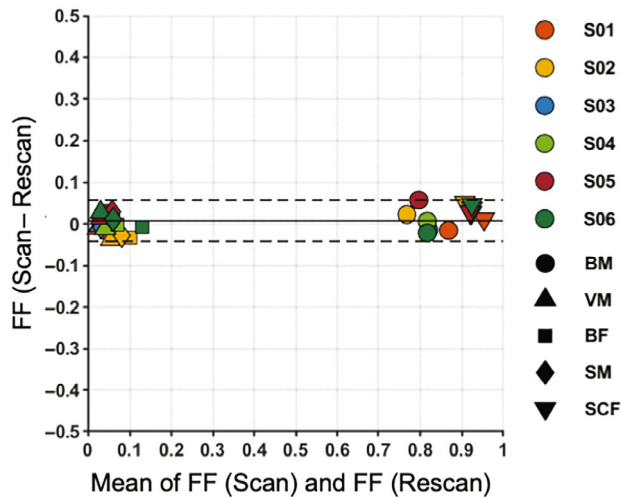
FIGURE 8 Scan-rescan repeatability of the FFs estimated with SPARCQ. Bland-Altmann analysis of scan-rescan repeatability in six volunteers (one volunteer = one color) for five regions of interest (one marker type = one region). Limits of agreement: LOA = 0.0074 ± 1.96 × 0.0574. Coefficient of repeatability: CR = 0.0512. BF, biceps femoralis; BM, bone marrow; SCF, subcutaneous fat; SM, semimembranous muscle; VM, vastus medialis.

to the ground truth values. However, the water-fat separation algorithm used in the ME-GRE approach relied on fixed peak locations and amplitudes of fat obtained from phantom ^{1}H MRS at 9.4T, whereas SPARCQ did not require a fixed spectral model. While the flexibility of not using a fixed spectral model is an advantage of SPARCQ, the current implementation underestimates fat because the three fat resonances around the water peak are incorrectly assigned to the water compartment. In future work, straightforward corrections can be implemented, because fat peaks resonating close to water are a fixed proportion of the total peak area of fat. The possibility of such a correction was demonstrated by the agreement of SPARCQ fraction estimates with a fraction based on a chemical shift threshold, the FF(CST) (Figure 4C versus Figure 4D). This alternative metric provided a better indication of the performance of SPARCQ because it takes into account the assignment of fat peaks resonating near water to the water compartment. Therefore, in the absence of a spectral fat model, this metric demonstrated that SPARCQ has the capability to distinguish compartments based on their resonance frequency and has the potential to accurately quantify FF. Nevertheless, the sensitivity of SPARCQ to detect and differentiate individual fat resonance peaks was not investigated and is subject to future studies.

Volunteer experiments confirmed that SPARCQ, as expected in the current implementation, underestimated FF compared with ME-GRE. These experiments also demonstrated the repeatability of SPARCQ. In

vivo quantitative maps showed the expected contrast between fatty and non-fatty regions. M_0-weighted water-fat-separated images obtained with SPARCQ compared well with those obtained with reference Dixon techniques. Nonetheless, SPARCQ maps and images showed that in some tissue regions close to air-tissue interfaces (e.g., in the patella) fat was misclassified. This was caused by the rigid peak selection strategy applied to the frequency spectra, which assumes that the most on-resonance peak is water, which fails in the presence of strong B_0 inhomogeneities. Future studies will focus on using additional SPARCQ characteristics, such as the peak width in the frequency spectrum, to facilitate a B_0 independent peak assignment of fat and water. For example, fat can typically be identified as a broader peak in the frequency spectrum within each voxel (Figure 7). Alternatively, approaches similar to those used to mitigate strong B_0 inhomogeneities for water-fat separation in ME-GRE data could potentially be extended to SPARCQ.[16]

The potential to quantify FFs using asymmetries in the bSSFP profile has several advantages over current techniques. The first is that bSSFP MRI provides a higher SNR compared with GRE-based MRI techniques. Second, because of the bSSFP T_1/T_2 -contrast, the potential T_1 signal bias that can be observed with ME-GRE may be reduced. While current results do not suggest the presence of signal bias, further evaluation and quantification of potential sources of signal bias and to what extent they may be mitigated within the SPARCQ framework are needed. This includes investigating the impact of B_1 and magnetization transfer effects, which can be modeled as a T_1 variation.[52] Third, SPARCQ does not suffer from T_2^* signal decay, as observed in ME-GRE, and assumptions on T_2^* signal decay are not needed compared with current water-fat separation algorithms. The last advantage is that SPARCQ has the potential to quantify fat without using strict assumptions on the underlying fat spectrum, in terms of chemical shift of the expected fat peaks and their amplitudes.

Approximating an acquired signal profile as a weighted sum of multiple dictionary entries rather than finding the best matched single dictionary entry has recently been proposed,[49,50] and was extended to two dimensions in the current work. This approach provides various benefits: (1) It minimizes the dimensionality of the dictionary, thus speeding up the processing and reducing the memory footprint of the algorithm. (2) It relies on simple signal models, where bSSFP profiles are simulated for a single combination of frequency (df) and relaxation time ratio (Λ), without requiring prior knowledge of the location, amount, and amplitudes of the different spectral components of water and fat. Nevertheless, the current dictionary matching approach is relatively slow in terms of

reconstruction speed, and the current voxel-wise approach does not consider nor leverage neighboring voxel information. In addition, the phase augmentation step, albeit fast, could be incorporated in the matching process with a spatial smoothness constraint in future implementations. This, together with exploiting joint sparsity constraints[53] may help to accelerate the reconstruction and increase the resolution of the dictionary.

The current work was intended to demonstrate the feasibility of our concept rather than optimizing for speed or resolution. The bSSFP profile was measured by performing 36 fully-sampled phase-cycled bSSFP acquisitions. Therefore, the resulting acquisition time of 20 min is significantly higher compared to the ME-GRE acquisition of 3 min. Studies, similar as those performed in single compartments for quantitative mapping with PC-bSSFP,[54] will need to be performed in order to define the minimum required phase-cycled scans for water-fat-quantification. Furthermore, the effect of changing TR was not investigated. To quantify fat through profile asymmetries, the TR should be well above 2.2 ms and well below 4.5 ms to preserve asymmetries in the bSSFP profile at 3T (Figure S1 in Data S1). Shortening scan time by TR reduction is thus feasible, but will affect the bandwidth of the resulting off-resonance spectrum. This illustrates an intricate relationship between asymmetry sampling and detection that requires further studies that fell outside of the scope of the present work. For example, asymmetry sampling could be improved by including signal profiles like those obtained with fast interrupted steady state sequences.[55,56] Asymmetry detection could be improved by optimizing the RF excitation angle to find a better trade-off between SNR of different tissue types, while preserving signal asymmetries. For example, the current study focused on fat estimation and displayed rather low SNR in the water-only images.

The current study demonstrates the potential to quantify fat based on asymmetries observed in the phase-cycled bSSFP profile. The off-resonance encoding of steady-state magnetization, with phase-cycled bSSFP, may become a powerful alternative for FF quantification, overcoming challenges of established time-domain encoding methods.

5 | CONCLUSIONS

SPARCQ is a novel quantitative method for detection of different tissue components within the same voxel. This proof-of-concept study demonstrated the potential for voxel-wise water-fat separation and quantification by using asymmetries observed in the phase-cycled bSSFP signal profile. SPARCQ showed noise robustness, accuracy, and repeatability corroborated by simulations,

phantom and volunteer experiments, and may be a promising alternative to conventional proton density FF estimation techniques.

CONFLICT OF INTEREST STATEMENT
Several authors are inventors of a patent related to the proposed development.[57] Tom Hilbert and Tobias Kober are employed by Siemens Healthineers International AG.

DATA AVAILABILITY STATEMENT
The acquired data from phantoms and volunteers is publicly available and can be found on the following repository: https://zenodo.org/record/7789414#.ZCb5uXZBzcs.

ORCID
Giulia M. C. Rossi https://orcid.org/0009-0009-8492-9557
Tom Hilbert https://orcid.org/0000-0001-8207-4908
Jessica A. M. Bastiaansen https://orcid.org/0000-0002-5485-1308

REFERENCES
1. Reeder SB, Cruite I, Hamilton G, Sirlin CB. Quantitative assessment of liver fat with magnetic resonance imaging and spectroscopy. *J Magn Reson Imaging*. 2011;34:729-749. doi:10.1002/jmri.22580
2. Reeder SB, Robson PM, Yu H, et al. Quantification of hepatic steatosis with MRI: the effects of accurate fat spectral modeling. *J Magn Reson Imaging JMRI*. 2009;29:1332-1339. doi:10.1002/jmri.21751
3. Tang A, Tan J, Sun M, et al. Nonalcoholic fatty liver disease: MR imaging of liver proton density fat fraction to assess hepatic steatosis. *Radiology*. 2013;267:422-431. doi:10.1148/radiol.12120896
4. Kellman P, Hernando D, Arai AE. Myocardial fat imaging. *Curr Cardiovasc Imaging Rep*. 2010;3:83-91. doi:10.1007/s12410-010-9012-1
5. Sharma S, Adrogue JV, Golfman L, et al. Intramyocardial lipid accumulation in the failing human heart resembles the

lipotoxic rat heart. *FASEB J off Publ Fed Am Soc Exp Biol.* 2004;18:1692-1700. doi:10.1096/fj.04-2263com

6. Griffith JF, Yeung DKW, Antonio GE, et al. Vertebral bone mineral density, marrow perfusion, and fat content in healthy men and men with osteoporosis: dynamic contrast-enhanced MR imaging and MR spectroscopy. *Radiology.* 2005;236:945-951. doi:10.1148/radiol.2363041425

7. Griffith JF, Yeung DKW, Antonio GE, et al. Vertebral marrow fat content and diffusion and perfusion indexes in women with varying bone density: MR evaluation. *Radiology.* 2006;241:831-838. doi:10.1148/radiol.2413051858

8. Pichardo JC, Milner RJ, Bolch WE. MRI measurement of bone marrow cellularity for radiation dosimetry. *J Nucl Med.* 2011;52:1482-1489. doi:10.2967/jnumed.111.087957

9. Reeder SB, Hu HH, Sirlin CB. Proton density fat-fraction: a standardized MR-based biomarker of tissue fat concentration. *J Magn Reson Imaging JMRI.* 2012;36:1011-1014. doi:10.1002/jmri.23741

10. Dixon WT. Simple proton spectroscopic imaging. *Radiology.* 1984;153:189-194.

11. Ma J. Dixon techniques for water and fat imaging. *J Magn Reson Imaging.* 2008;28:543-558. doi:10.1002/jmri.21492

12. Hernando D, Haldar JP, Sutton BP, Ma J, Kellman P, Liang ZP. Joint estimation of water/fat images and field inhomogeneity map. *Magn Reson Med.* 2008;59:571-580. doi:10.1002/mrm.21522

13. Karampinos DC, Melkus G, Baum T, Bauer JS, Rummeny EJ, Krug R. Bone marrow fat quantification in the presence of trabecular bone: initial comparison between water-fat imaging and single-voxel MRS: bone marrow fat quantification. *Magn Reson Med.* 2014;71:1158-1165. doi:10.1002/mrm.24775

14. Kellman P, Hernando D, Shah S, et al. Multiecho Dixon fat and water separation method for detecting fibrofatty infiltration in the myocardium. *Magn Reson Med.* 2009;61:215-221. doi:10.1002/mrm.21657

15. Hu HH, Börnert P, Hernando D, et al. ISMRM workshop on fat–water separation: insights, applications and progress in MRI. *Magn Reson Med.* 2012;68:378-388. doi:10.1002/mrm.24369

16. Hernando D, Kellman P, Haldar JP, Liang ZP. Robust water/-fat separation in the presence of large field inhomogeneities using a graph cut algorithm. *Magn Reson Med.* 2010;63:79-90. doi:10.1002/mrm.22177

17. Mackowiak ALC, Roy CW, Yerly J, et al. Motion-resolved fat-fraction mapping with whole-heart free-running multiecho gre and pilot tone. 2022. doi:10.48550/arXiv.2210.06127

18. Ostenson J, Damon BM, Welch EB. MR fingerprinting with simultaneous T_1, T_2, and fat signal fraction estimation with integrated B_0 correction reduces bias in water T_1 and T_2 estimates. *Magn Reson Imaging.* 2019;60:7-19. doi:10.1016/j.mri.2019.03.017

19. Cencini M, Biagi L, Kaggie JD, Schulte RF, Tosetti M, Buonincontri G. Magnetic resonance fingerprinting with dictionary-based fat and water separation (DBFW MRF): a multi-component approach. *Magn Reson Med.* 2019;81:3032-3045. doi:10.1002/mrm.27628

20. Jaubert O, Arrieta C, Cruz G, et al. Multi-parametric liver tissue characterization using MR fingerprinting: simultaneous T_1, T_2, T_2^*, and fat fraction mapping. *Magn Reson Med.* 2020;84:2625-2635. doi:10.1002/mrm.28311

21. Jaubert O, Cruz G, Bustin A, et al. Water–fat Dixon cardiac magnetic resonance fingerprinting. *Magn Reson Med.* 2020;83:2107-2123. doi:10.1002/mrm.28070

22. Liu CY, McKenzie CA, Yu H, Brittain JH, Reeder SB. Fat quantification with IDEAL gradient echo imaging: correction of bias from T1 and noise. *Magn Reson Med.* 2007;58:354-364. doi:10.1002/mrm.21301

23. Yang IY, Cui Y, Wiens CN, Wade TP, Friesen-Waldner LJ, McKenzie CA. Fat fraction bias correction using T_1 estimates and flip angle mapping. *J Magn Reson Imaging.* 2014;39:217-223. doi:10.1002/jmri.24126

24. Kühn JP, Hernando D, Muñoz del Rio A, et al. Effect of multipeak spectral modeling of fat for liver iron and fat quantification: correlation of biopsy with MR imaging results. *Radiology.* 2012;265:133-142. doi:10.1148/radiol.12112520

25. Yu H, Shimakawa A, McKenzie CA, Brodsky E, Brittain JH, Reeder SB. Multiecho water-fat separation and simultaneous R estimation with multifrequency fat spectrum modeling. *Magn Reson Med.* 2008;60:1122-1134. doi:10.1002/mrm.21737

26. Bieri O, Scheffler K. Fundamentals of balanced steady state free precession MRI. *J Magn Reson Imaging.* 2013;38:2-11. doi:10.1002/jmri.24163

27. Scheffler K, Lehnhardt S. Principles and applications of balanced SSFP techniques. *Eur Radiol.* 2003;13:2409-2418. doi:10.1007/s00330-003-1957-x

28. Smith TB, Nayak KS. MRI artifacts and correction strategies. *Imaging Med.* 2010;2:445-457. doi:10.2217/iim.10.33

29. Bangerter NK, Hargreaves BA, Vasanawala SS, Pauly JM, Gold GE, Nishimura DG. Analysis of multiple-acquisition SSFP. *Magn Reson Med.* 2004;51:1038-1047. doi:10.1002/mrm.20052

30. Cukur T, Lustig M, Nishimura DG. Multiple-profile homogeneous image combination: application to phase-cycled SSFP and multicoil imaging. *Magn Reson Med.* 2008;60:732-738. doi:10.1002/mrm.21720

31. Xiang QS, Hoff MN. Banding artifact removal for bSSFP imaging with an elliptical signal model. *Magn Reson Med.* 2014;71:927-933. doi:10.1002/mrm.25098

32. Björk M, Ingle RR, Gudmundson E, Stoica P, Nishimura DG, Barral JK. Parameter estimation approach to banding artifact reduction in balanced steady-state free precession. *Magn Reson Med.* 2014;72:880-892. doi:10.1002/mrm.24986

33. Hilbert T, Nguyen D, Thiran JP, Krueger G, Kober T, Bieri O. True constructive interference in the steady state (trueCISS). *Magn Reson Med.* 2018;79:1901-1910. doi:10.1002/mrm.26836

34. Miller KL. Asymmetries of the balanced SSFP profile. Part I: theory and observation. *Magn Reson Med.* 2010;63:385-395. doi:10.1002/mrm.22212

35. Miller KL, Smith SM, Jezzard P. Asymmetries of the Balanced SSFP Profile. part II: White matter. *Magn Reson Med.* 2010;63:396-406. doi:10.1002/mrm.22249

36. Nguyen D, Bieri O. Motion-insensitive rapid configuration relaxometry. *Magn Reson Med.* 2017;78:518-526. doi:10.1002/mrm.26384

37. Ehses P, Báez-Yánez M, Erb M, Scheffler K. Asymmetries of the balanced SSFP profile allow to probe microstructure anisotropy at 9.4 tesla. *Proc Intl Soc Mag Reson Med.* 2017;25:993.

38. Schäper J, Bauman G, Ganter C, Bieri O. Pure balanced steady-state free precession imaging (pure bSSFP). *Magn Reson Med.* 2022;87:1886-1893. doi:10.1002/mrm.29086

39. Birk F, Glang F, Loktyushin A, et al. High-resolution neural network-driven mapping of multiple diffusion metrics leveraging asymmetries in the balanced steady-state free precession frequency profile. *NMR Biomed*. 2022;35:e4669. doi:10.1002/nbm.4669

40. Heule R, Deshmane A, Zaiss M, Herz K, Ehses P, Scheffler K. Structure or exchange? On the feasibility of chemical exchange detection with balanced steady-state free precession in tissue-an In vitro study. *NMR Biomed*. 2020;33:e4200. doi:10.1002/nbm.4200

41. Vasanawala SS, Pauly JM, Nishimura DG. Linear combination steady-state free precession MRI. *Magn Reson Med*. 2000;43:82-90. doi:10.1002/(SICI)1522-2594(200001)43:1<82::AID-MRM10>3.0.CO;2-9

42. Çukur T, Bangerter NK, Nishimura DG. Enhanced spectral shaping in steady-state free precession imaging. *Magn Reson Med*. 2007;58:1216-1223. doi:10.1002/mrm.21413

43. Cukur T, Nishimura DG. Fat-water separation with alternating repetition time balanced SSFP. *Magn Reson Med*. 2008;60:479-484. doi:10.1002/mrm.21692

44. Cukur T, Yamada M, Overall WR, Yang P, Nishimura DG. Positive contrast with alternating repetition time SSFP (PARTS): a fast imaging technique for SPIO-labeled cells. *Magn Reson Med*. 2010;63:427-437. doi:10.1002/mrm.22241

45. Çukur T. Spectrally selective imaging with wideband balanced steady-state free precession MRI. *Magn Reson Med*. 2016;75:1132-1141. doi:10.1002/mrm.25700

46. Mackowiak ALC, Hilbert T, Rossi GMC, Kober T, Bastiaansen JAM. Optimized fast fat-fraction mapping in the knee using Signal Profile Asymmetries for Robust multi-Compartment Quantification (SPARCQ). *Proc Intl Soc Mag Reson Med*. 2020;28:3229.

47. Deshpande VS, Chung YC, Zhang Q, Shea SM, Li D. Reduction of transient signal oscillations in true-FISP using a linear flip angle series magnetization preparation. *Magn Reson Med*. 2003;49:151-157. doi:10.1002/mrm.10337

48. Ma D, Gulani V, Seiberlich N, et al. Magnetic resonance fingerprinting. *Nature*. 2013;495:187-192. doi:10.1038/nature11971

49. Canales-Rodríguez EJ, Pizzolato M, Piredda GF, et al. Comparison of non-parametric T_2 relaxometry methods for myelin water quantification. *Med Image Anal*. 2021;69:101959. doi:10.1016/j.media.2021.101959

50. Piredda GF, Hilbert T, Canales-Rodríguez EJ, et al. Fast and high-resolution myelin water imaging: accelerating multi-echo GRASE with CAIPIRINHA. *Magn Reson Med*. 2021;85:209-222. doi:10.1002/mrm.28427

51. Bush EC, Gifford A, Coolbaugh CL, Towse TF, Damon BM, Welch EB. Fat-water phantoms for magnetic resonance imaging validation: a flexible and scalable protocol. *J Vis Exp*. 2018;139:57704. doi:10.3791/57704

52. Bieri O, Scheffler K. On the origin of apparent low tissue signals in balanced SSFP. *Magn Reson Med*. 2006;56:1067-1074. doi:10.1002/mrm.21056

53. Nagtegaal M, Koken P, Amthor T, Doneva M. Fast multi-component analysis using a joint sparsity constraint for MR fingerprinting. *Magn Reson Med*. 2019;83:521-534. doi:10.1002/mrm.27947

54. Keskin K, Yılmaz U, Çukur T. Constrained ellipse fitting for efficient parameter mapping with phase-cycled bSSFP MRI. *IEEE Trans Med Imaging*. 2022;41:14-26. doi:10.1109/TMI.2021.3102852

55. Koktzoglou I, Edelman RR. Radial fast interrupted steady-state (FISS) magnetic resonance imaging. *Magn Reson Med*. 2018;79:2077-2086. doi:10.1002/mrm.26881

56. Bastiaansen JAM, Piccini D, Sopra LD, et al. Natively fat-suppressed 5D whole-heart MRI with a radial free-running fast-interrupted steady-state (FISS) sequence at 1.5T and 3T. *Magn Reson Med*. 2020;83:45-55. doi:10.1002/mrm.27942

57. Hilbert T, Kober T, Rossi GMC, Bastiaansen JAM. Method and System for Mapping a Fraction of Tissue Concentrations in MRI. 2021; (EP20200152927 20200121) https://lens.org/052-110-577-103-48X, https://lens.org/147-743-972-727-940, https://worldwide.espacenet.com/publicationDetails/biblio?FT=D&date=20210722&DB=&locale=en_EP&CC=US&NR=2021224982A1&KC=A1&ND=4 Accessed November 22, 2022.

SUPPORTING INFORMATION

Additional supporting information may be found in the online version of the article at the publisher's website.

Data S1. Supporting information.